Analysis of Facility Thermodynamic Non-Equilibrium Effects on HIFiRE Ground Tests

R. A. Baurle
Hypersonic Airbreathing Propulsion Branch
NASA Langley Research Center
Hampton, Va 23681

ABSTRACT

The HIFiRE Flight 2 experiment proved to be an extremely successful research effort, and Computational Fluid Dynamics (CFD) played a crucial role in this success. In particular, CFD was used to design and analyze the forebody and inlet of the research payload without the aid of any ground testing. Moreover, the only ground tests performed were direct-connect combustor tests, which forced the reliance on CFD to bridge the entire gap from direct-connect ground tests to flight. Historically, this role has relied heavily on semi-freejet and freejet testing. The closure models for the Reynolds-averaged equations that govern turbulent reacting flows contain a high degree of empiricism and typically require some level of calibration using experimental measurements at relevant conditions prior to being used as a predictive tool. The direct-connect ground tests used for the calibration of the HIFiRE CFD effort were performed in the Arc-Heated Scramjet Test Facility located at the NASA Langley Research Center. This facility introduces flow conditions to the scramjet test article that contain some level of thermal non-equilibrium. The thermal non-equilibrium effects (in the form of vibrational freezing) proved to have a non-negligible impact on the thermodynamic state of the flow entering the isolator, particularly at the Mach 8 flight test conditions. This complicated the calibration effort since the CFD analysis performed at the time utilized a thermal equilibrium gas model. The impact of thermal non-equilibrium was studied in this effort through the use of a two-temperature formulation (translational/rotational and vibrational/electronic temperatures) that has recently been added to the VULCAN-CFD code. Overall, comparisons with surface pressure measurements in the isolator (upstream of the pre-combustion shock system) improved significantly when vibrational freezing was accounted for. The pre-combustion shock train location was also in better agreement with the measurements as compared to the results obtained when thermal equilibrium was assumed. However, the calibrated CFD model that provided a "best fit" to the ground test data based on the thermal non-equilibrium simulations was nearly identical to that derived from the thermally equilibrated simulations used in previous efforts. Hence, the present findings do not significantly alter the ground-to-flight mapping used for the HIFiRE Flight 2 CFD predictions.

NOMENCLATURE

Symbols

A	cross sectional area
A_{mn}	1st coefficient of the Millikan and White correlation
B_{mn}	2nd coefficient of the Millikan and White correlation

---

C_p	specific heat at constant pressure (per mass)
C_{pd}	preferential dissociation coefficient
D	diffusion coefficient
$\hat{D}$	vibrational energy created/destroyed by chemical processes
e	energy (per mass)
h	enthalpy (per mass) or isolator height
$\hat{I}$	first ionization energy (per mole)
k	thermal conductivity
$\dot{m}$	mass flow rate
n_j	unit normal vector
ni	number of ionized species
nm	number of molecules
ns	number of species (excluding electrons)
$\dot{n}$	ionization rate (mole-based)
P_r	Prandtl number
P_o^{rec}	total pressure recovery
p	pressure
Q_{rad}	radiative energy transfer rate
q_j	heat flux vector
S_c	Schmidt number
s	entropy (per mass)
T	temperature
t	surface thickness
u_j	velocity vector
W	molecular weight
$\dot{w}$	chemical production rate (mass-based)
x_j	Cartesian position vector
Y	species mass fraction
η_c	combustion efficiency
θ	characteristic temperature
μ	molecular viscosity or reduced molecular mass
$v_{e,m}$	effective collision frequency of electrons with species m
ρ	density
τ	translation/vibration relaxation time

Subscripts

e	electronic mode or electron
m, n	species indices
r	rotational mode
t	translational mode or turbulent quantity
tr	equilibrated translational/rotational mode
v	vibrational mode
ve	equilibrated vibrational/electronic mode

Superscripts

$^{-}$	standard time average
$\sim$	density-weighted time average
$''$	Favre fluctuation
$*$	equilibrium value

INTRODUCTION

The HIFiRE Direct Connect Rig (HDCR), was developed to provide pre-flight verification of propulsion system flowpath performance and operability across the HIFiRE (Flight 2) flight regime. [1] The HDCR is a full-scale, heat sink test article that duplicates both the flowpath lines, and a majority of the instrumentation layout of the isolator and combustor portion of the HIFiRE flight test hardware. The HDCR hardware was installed and tested in the NASA Langley Arc-Heated Scramjet Test Facility (AHSTF). The primary objectives of the HDCR test series were to:

- verify that the isolator/combustor portion of the HIFiRE flowpath demonstrated satisfactory operability (with margin) spanning the transition from dual-mode to scram-mode operation

- identify a viable fuel schedule for both dual-mode and scram-mode operation (and the transition between the two modes of operation during vehicle acceleration)

- provide data to benchmark analytical tools used for flight performance and operability predictions

Given that the HDCR is a direct-connect test model, the AHSTF flow conditions are meant to replicate (in a 1-D sense) the isolator entrance conditions that result from the aerodynamic processing of the freestream flow by the forebody and inlet portions of the flight vehicle. Three facility nozzles were utilized to provide exit Mach numbers that matched the 1-D isolator entrance Mach numbers for the Mach 6, 7, and 8 flight conditions. While testing in a direct-connect facility is sufficient to satisfy the objectives of the HDCR test series outlined above, some aspects of the flight flow physics are inevitably compromised. Examples of detailed flight vehicle flow features that are not matched in the HDCR ground tests include:

- flow distortion from the forebody and inlet compression processes is not present

- surface boundary layers are significantly thinner than those present in flight

- surface temperature time history (and associated heat loads)

- air composition (up to 3% by mole of nitric oxide is produced by the arc-heating process which depletes the oxygen content by up to 1.5%)

- level of thermodynamic equilibration (vibrational freezing due to expansion processes in the facility nozzles are not present in flight)

The last two features represent facility vitiate effects that are specific to arc-heated facilities, but all high-enthalpy ground test facilities introduce some level of vitiation into the flowpath. For instance, combustion-heated facilities introduce water vapor (and possibly carbon dioxide) into the flow, which alters both the thermodynamic state of the "air" flow (primarily through higher heat capacity) and the chemical kinetics of fuel-air combustion processes. A discussion of the various vitiate effects that are present for different classes of high-enthalpy ground test facilities can be found in Refs. [2–7]. Note that most of the blow-down test facilities currently in use for scramjet testing are combustion-heated facilities. As a result, the effects of vitiates present in these facilities have been more widely studied than those that are produced in arc-heated facilities. Moreover, vibrational freezing is not a factor in these facilities due to the water vapor present in the air stream, which is known to promote rapid vibrational relaxation towards thermal equilibrium. Vibrational non-equilibrium is a more prevalent issue in higher Mach number facilities (Mach 10+). Examples of computational efforts aimed at quantifying the effects of vibrational non-equilibrium can be found in Refs. [8] and [9].

The HIFiRE Flight 2 project relied on CFD data to an extent not seen in any previous scramjet flight test program. The forebody and inlet components for the payload were designed via CFD tools, and all inlet performance and operability metrics were quantified using CFD data (and other analytical tools) without

any verification via ground test data. This made the quantification of uncertainties associated with the CFD simulation data a top priority during the pre-flight analyses. Particular attention was given towards the prediction of isolator margin; a measure of how robust an engine is to a combustion-induced engine unstart. The ability to predict the isolator margin was critical to the success of the flight experiment, since an unstarted flowpath during flight would have jeopardized the successful achievement of the flight science objectives. The ground-to-flight dual-mode operability prediction process has been documented in detail in Ref. [10], but the overall process that was used can be summarized as follows:

1. collect ground test data and identify (and quantify) the uncertainties resulting from facility operation, testing methods, and hardware

2. calibrate CFD analysis tools to ground test data using the turbulent Schmidt number, S_{c_t}, as the free parameter, and identify the largest remaining contributors to the CFD modeling uncertainty

3. execute a ground test design of experiments (DOE) matrix to derive a response surface equation (RSE) for dual-mode ground test isolator operability

4. assume that the calibrated CFD model is also well calibrated to flight conditions

5. execute a pre-flight design of experiments DOE matrix (based on flight system and trajectory uncertainties) to derive an RSE for dual-mode isolator operability of the flight payload

Clearly, the success of this approach to the ground-to-flight mapping hinges on the accuracy of the assumption stated in Step 4 of this process. This step could not even be partially verified for this project due to the lack of any freejet or semi-freejet ground testing of the flight payload. Hence, this was a known (but accepted) risk prior to flight.

The HDCR CFD simulation data collected in the calibration process relied on thermal equilibrium gas models since the CFD tools used at the time did not have the capability to consider thermal non-equilibrium effects. This deficiency had the potential to compromise the assumption that "*the calibrated ground-test CFD model is also well calibrated for flight*" since the calibrated S_{c_t} value (a parameter that governs the rate of turbulent mixing) may have incorrectly compensated for deficiencies in the thermodynamic model. The present effort was initiated to address this issue. In particular, this work was undertaken to determine the impact of vibrational freezing on the surface pressures and performance measures of the HDCR flowpath, as well as the impact on the calibrated S_{c_t} value carried forward for the flight simulations (where vibrational freezing is not present).

VIBRATIONAL NON-EQUILIBRIUM MODEL

Flows that are not thermally equilibrated (*i.e.* the distribution of energy between translational, rotational, vibrational, and electronic modes can not be described by a single temperature), require the introduction of additional transport equations for those energy modes that are not equilibrated with the translational energy. The cost of solving these additional equations together with the limited availability of physical constants that describe the finite-rate processes associated with the transfer of energy amongst the various modes are important factors that must be considered when developing engineering tools for these flows. Historically, the development of the VULCAN-CFD code [11, 12] has been driven by the needs of the scramjet community, which often requires the consideration of complicated polyatomic molecules (*e.g.* heavy hydrocarbons), or even JP fuels that are basically "hydrocarbon soups" with an unspecified molecular distribution that simply satisfy certain specified combustion properties. This reality, together with the understanding that most scramjet applications are bounded below Mach 10-12 flight, prompted the consideration of a simple two-temperature thermal non-equilibrium model. [13] This formulation assumes that the translation and rotational energy modes are equilibrated at a single temperature T_{tr}, while the vibrational and electronic energy modes are equilibrated at temperature T_{ve}. From a scramjet facility perspective (the focus of this effort), this level

of modeling is appropriate for dealing with any vibrational freezing that may be present in supersonic (or hypersonic) facility nozzles.

The Reynolds-averaged equation that governs the evolution of the equilibrated vibrational/electronic energy can be written as follows:

$$
\underbrace{\frac{\partial}{\partial t}\left(\bar{\rho}\tilde{e}_{ve}\right)}_{1} + \underbrace{\frac{\partial}{\partial x_j}\left(\bar{\rho}\tilde{e}_{ve}\tilde{u}_j + \bar{\rho}\widetilde{e_{ve}''u_j''}\right)}_{2} = \underbrace{-\frac{\partial \bar{q}_{ve_j}}{\partial x_j}}_{3} + \underbrace{\sum_{m=1}^{nm}\overline{\rho_m\left(\frac{e_{ve,m}^* - e_{ve,m}}{\tau_m}\right)}}_{4} + \underbrace{\sum_{m=1}^{nm}\overline{\dot{w}_m\hat{D}_m}}_{5} -
$$

$$
\underbrace{\overline{p_e\frac{\partial u_j}{\partial x_j}}}_{6} + \underbrace{2\,\overline{\rho_e\frac{3}{2}\left(T - T_{ve}\right)\sum_{m=1}^{ns}\frac{\nu_{e,m}}{W_m}}}_{7} - \underbrace{\sum_{m=1}^{ni}\overline{\dot{n}_{e,m}\hat{I}_m}}_{8} - \underbrace{\overline{Q}_{rad}}_{9} \qquad (1)
$$

Term (1) represents the time rate of change of the vibrational/electronic energy, e_{ve}. Term (2) accounts for the convection (mean and turbulent) of e_{ve}. Term (3) contains the molecular diffusion processes of the vibrational/electronic energy. Term (4) represents the energy exchange between the vibrational and translational modes due to molecular collisions. Term (5) represents the vibrational energy that is lost (or gained) due to the molecular depletion (dissociation) or production (recombination) that result from chemical kinetics. Term (6) is a term that accounts for the combined effect of the convection of electron pressure and the work done on electrons by the electric field induced by the electron pressure gradient. Term (7) accounts for the energy exchange due to elastic collisions between free electrons and atoms/molecules. Term (8) represents the electronic energy loss due to electron impact ionization. Finally, Term (9) accounts for the loss of electronic energy due to radiation caused by electronic transitions. The specific models used to close Eq. 1 for this effort are given in Appendix A along with other implementation details. A more comprehensive discussion of the various models proposed in the literature can be found in Ref. [13].

MODEL VALIDATION

A model validation effort was undertaken prior to applying the thermal non-equilibrium formulation to the HDCR configuration. Recent Dual-Pump Coherent Anti-Stokes RAMAN Spectroscopy (DP-CARS) measurements [14] have been made in the Scramjet Combustion Facility (SCF) located at the University of Virginia. This facility is a direct-connect, electrical-resistance-heated facility capable of providing continuous air flow with a total temperature of up to 1200 K. This facility also has the capability to add controlled levels of steam and/or carbon dioxide to examine the effects of vitiation. The facility nozzle used for this research effort is a symmetric two-dimensional contoured nozzle with an area ratio of 1.786. The width of the nozzle is 1.5 inches and the height at the nozzle exit is 1 inch. A constant area isolator connects the nozzle exit plane (located 1.97 inches downstream of the throat) to the combustor model used for the scramjet combustion experiments.

VULCAN-CFD simulations were performed for clean air (N_2 and O_2 mass fractions of 0.767 and 0.233) at a stagnation pressure and temperature of 296 kPa and 1200 K, respectively. The simulations were performed using the two-temperature thermal non-equilibrium model with the Millikan and White translation/vibration relaxation time parameters listed in Table 1 (these values were taken from the database distributed with the Langley Aerothermodynamic Upwind Relaxation Algorithm CFD code [13]). The simulation was advanced in pseudo-time using a Diagonalized Approximate Factorization (DAF) scheme [15] with a Courant-Friedrichs-Lewy (CFL) number of 2.5. The inviscid fluxes were evaluated using the Low-Dissipation Flux Split Scheme of Edwards, [16] and the viscous fluxes were evaluated with a centered scheme. The Menter BSL [17] model was chosen for turbulence closure with the turbulent Prandtl number (P_{r_t}) set to 0.9. The computational domain and the multi-block structured grid generated for this domain are shown in Fig. 1. The simulations took advantage of all available symmetries (*i.e.* only 1/4 of the full facility flow path was simulated). The grid consists of 1,361,920 cells with the grid clustered to all surfaces to maintain surface cell center y^+ values

near unity. A coarsened version of the grid (full factor of 2 coarsening in each coordinate direction) was also utilized to assess numerical errors. Specified stagnation conditions were applied at the entrance to the nozzle (Mach number extrapolated from the interior), 1st order extrapolation defined the supersonic outflow condition, and no-slip isothermal (wall temperature of 600 K) conditions were enforced on the surfaces. Figure 1 also illustrates several features of this nozzle flow. The computed Mach number contours (based on the translational/rotational specific heat) are shown in the top image, and vibrational/electronic (upper quadrant) and translational/rotational (lower quadrant) temperatures are shown in the bottom image. Some level of vibrational freezing is clearly evident by the near-constant vibrational/electronic temperatures shown in the core of the flow throughout the nozzle and isolator.

Table 1: Translation/Vibration Millikan and White relaxation time parameters

Molecule	A_{mN_2} , B_{mN_2}	A_{mO_2} , B_{mO_2}
N_2	220.0 , *	220.0 , *
O_2	129.0 , *	129.0 , *

* Denotes the default Millikan and White value for B_{mn}

The two-temperature model used for the simulations allows for a single vibrational/electronic temperature for all molecules in the mixture. In order to compare the simulation data with the DP-CARS measurements (which measures independent vibrational temperatures for N_2 and O_2), a mixture-averaged vibrational/electron temperature value was computed using the following expression:

$$Y_{N_2}\, e_{ve,N_2}(T_{ve})\ +\ Y_{O_2}\, e_{ve,O_2}(T_{ve})\ =\ Y_{N_2}\, e_{ve,N_2}(T_{ve,N_2})\ +\ Y_{O_2}\, e_{ve,O_2}(T_{ve,O_2}) \tag{2}$$

The temperatures from the VULCAN-CFD simulation are compared with the mixture-averaged DP-CARS measured values in Fig. 2. The comparison is made 13.9 inches downstream of the nozzle throat along the spanwise centerplane (see Fig. 1) of the facility. In the figure, all coordinates have been non-dimensionalized by the height of the isolator (h = 1 in). There were known spatial non-uniformities in the stagnation temperature of the flow exiting the facility heater, which is the reason for the decrease in the measured temperatures from the lower wall to the upper wall. The reported measurement uncertainties were ± 25 K for the rotational temperatures and ± 40 K for the vibrational temperatures. An estimate of the numerical uncertainty (*i.e.* grid convergence) for the simulation data was obtained using the Grid Convergence Index (GCI). [18] The GCI is a grid convergence estimator derived from the generalized Richardson extrapolation formula and can be written as follows:

$$\text{GCI} = F_s \frac{|\epsilon|}{r^p - 1} \tag{3}$$

In this expression, ϵ is the difference of some functional "f" evaluated using two different grid resolutions with refinement ratio r, and p is order of accuracy of the numerical scheme. Finally, F_s is a "factor of safety" with recommended values taken to be either 3 (if the observed order of accuracy is assumed to be the theoretical value) or 1.25 (if the observed order of accuracy has been rigorously determined). It should be emphasized that the GCI, while based on Richardson Extrapolation, is not meant to be a "best estimate" of the numerical error. Instead, the intent is to provide a reasonable bound on the discretization error. The numerical uncertainty bars are included (but barely discernible) on the simulated results shown in Fig. 2. The largest error (as a percentage of the fine grid temperature value) was 0.45% for the translational/rotational temperature and 0.16% for the vibrational/electronic temperature.

Overall, the simulations have captured the proper level of vibrational freezing in a bulk sense, but there are two notable discrepancies. In general, the mixture-averaged vibrational temperature is somewhat under-predicted. Although not shown, the DP-CARS measurements suggested that the vibrational temperature of N_2 froze at the stagnation temperature ($\approx$ 1200 K), while the vibrational temperature of O_2 froze closer to the sonic temperature ($\approx$ 1000 K). Capturing this phenomenon would require the consideration of an independent vibrational energy equation for each molecule. Given the limitations of the two-temperature formulation, the level agreement shown in Fig. 2 was deemed acceptable. The second discrepancy involves the measured values closest to the walls of the tunnel. The CFD data suggest that this location should be
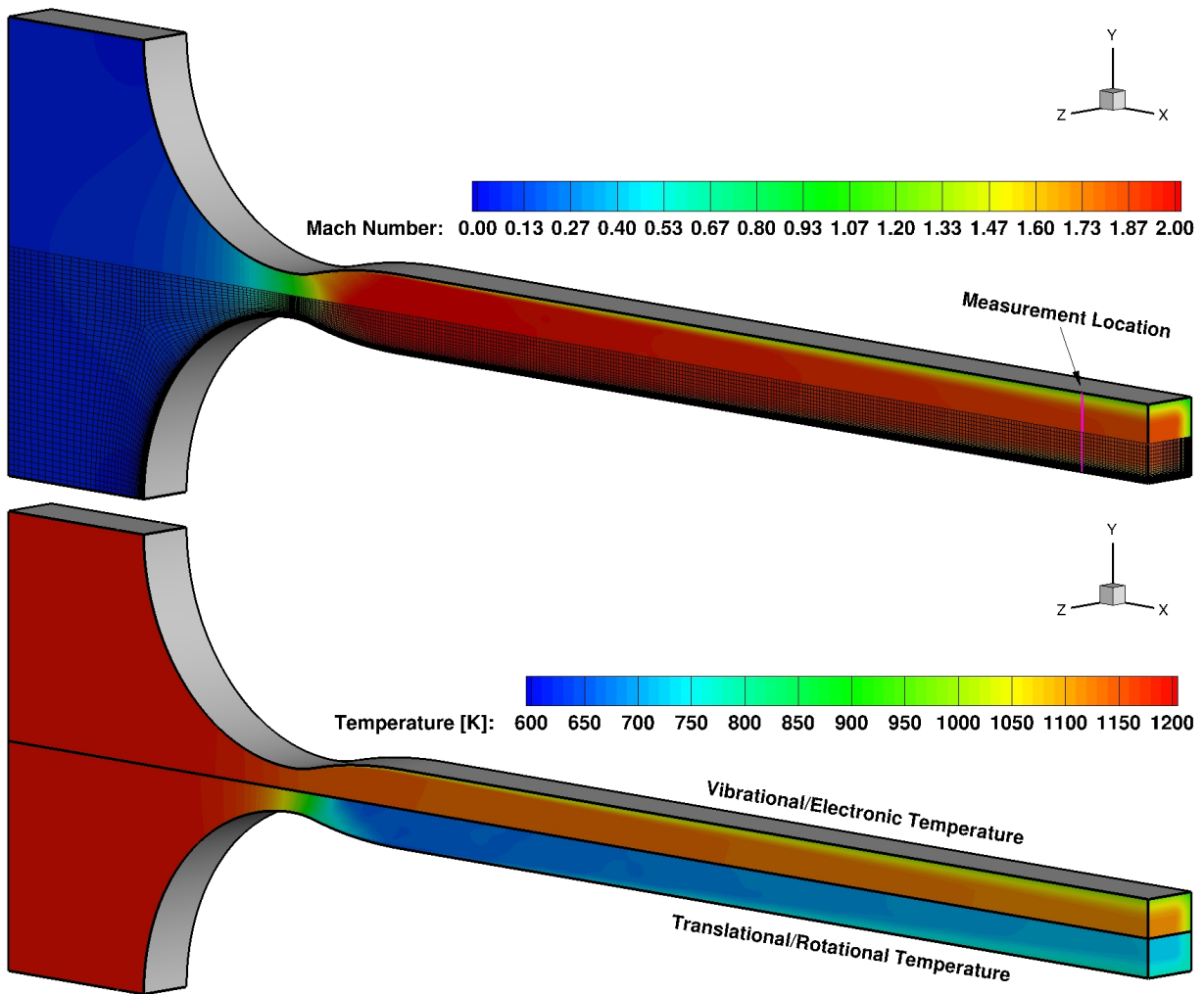
Figure 1: Computational grid and Mach number contours (top), vibrational/electronic and translational/rotational temperature contours (bottom) for the SCF flowfield

within the thermal boundary layer of the tunnel walls, hence a drop in the vibrational/electronic temperature was anticipated along with an increase in translational/rotational temperature (due to viscous heating). There were no detailed wall temperature measurements provided to define the wall thermal condition for the simulations, so this observation may suggest that the assumed value of 600 K requires some adjusting or that a significant degree of wall temperature variability was present. A larger P_{r_t} value may also be required to further reduce the thermal boundary layer thickness.
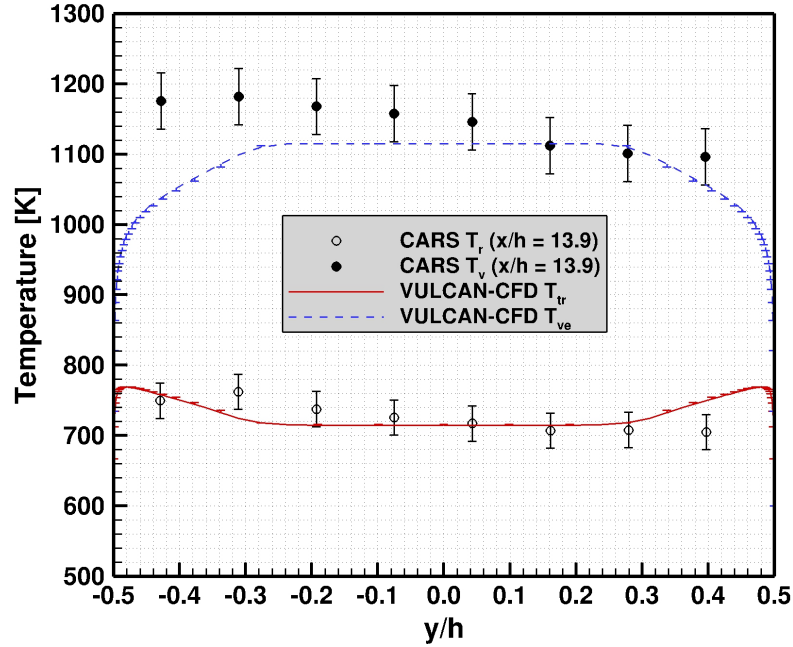
Figure 2: Comparison of measured and simulated temperatures along the tunnel centerplane at x/h=13.9

AHSTF FACILITY DESCRIPTION

A schematic of the AHSTF is shown in Fig. 3. The "main" air is heated by an electric arc, and then mixed with unheated "bypass" air in a plenum chamber to achieve a desired mixture stagnation enthalpy. Both the air mass flow rates and the plenum pressure are measured and recorded. The total mixed air stream is then expanded through a facility nozzle directly connected to the HDCR isolator entrance. The facility nozzles, designed to deliver the isolator entrance properties for Mach 6, 7, and 8 flight conditions, have design exit Mach numbers of 2.5, 3.0, and 3.5, respectively. The mixture stagnation enthalpy is calculated via a sonic throat method using the facility stagnation pressure, total mass flow rate, and nozzle throat area. [19] The facility fuel system delivers the fuel mixture surrogate for endothermically-cracked JP-7 (a molar mixture of 64% ethylene - 36% methane) to the test article. The fuel is heated upstream of the regulators and flow control valves as a cautionary measure to prevent condensation of the ethylene. Three separate legs from a single fuel manifold provide fuel to the injection stations in the combustor. The fuel flow rate is calculated via a choked flow expression using the stagnation pressure and temperature measurements upstream of a calibrated sonic venturi. The NIST software REFPROP16 [20] was used to determine the fuel properties required to compute the sonic mass flux for a given stagnation pressure and temperature. Turbine flow meters were also used for an independent check of the fuel flow rate. The fuel equivalence ratio is calculated assuming the test gas has a molar composition of 21% oxygen, 78% nitrogen, and 1% argon.

HDCR SIMULATION DESCRIPTION

The CFD data obtained in this effort were acquired by integrating the Reynolds-Averaged governing equations with either a thermal equilibrium or two-temperature non-equilibrium model until steady-state conditions were achieved. The simulations were advanced in pseudo-time using a Diagonalized Approximate Factorization (DAF) scheme [15] with a Courant-Friedrichs-Lewy (CFL) number of 2.5. The inviscid fluxes were evaluated using the Low-Dissipation Flux Split Scheme of Edwards [16] with cell interface variable reconstruction achieved via the κ=1/3 Monotone Upstream-centered Scheme for Conservation Laws. The van Leer flux limiter [21] was utilized to avoid spurious oscillations during this reconstruction process. The viscous fluxes were evaluated using 2nd-order accurate central differences with the species viscosities and conductivities computed from the polynomial fit of McBride. [22, 23] The Menter BSL [17] model was chosen for turbulence closure. The molecular and turbulent Prandtl numbers were set to 0.72 and 0.9, while the molecular and turbulent Schmidt numbers were set to 0.72 and 0.5. Combustion was modeled using the eddy dissipation concept of Magnussen and Hjertager, [24] which addresses turbulence-chemistry closure by assuming that the rate of reaction is limited by the rate of mixing between fuel and oxygen carrying eddies (rather than on the chemical kinetic time scale). All surfaces were treated as no-slip, non-catalytic surfaces with the exception of the secondary injector ports which utilized a slip wall treatment. The subsonic nozzle plenum inflow condition was specified via the measured plenum pressure and facility flow rate, with Mach number extrapolated from the interior. The inflow conditions for the angled primary fuel injection ports (labeled as P1 in Fig. 4) were defined given the measured fuel flow rate and stagnation temperature, with pressure extrapolated from the interior. The secondary injection ports (labeled as S1 in Fig. 4) were specified as sonic orifices. Finally, all properties were extrapolated at the supersonic exit of the combustor.

The computational domain considered spans the region from the start of the facility nozzle to the end of the HDCR combustor (see Fig. 4). The symmetry present in this geometry, and the fact that only steady-state simulations were of interest, permitted the simulation of only one quarter of the facility flowpath. A structured grid with a total of 7,675,904 cells was created for the simulations. A coarser grid (959,488 cells) was obtained from this parent grid via a factor of 2 coarsening in each coordinate direction to allow for an assessment of the numerical errors. The entire grid was split up into a total of 1539 grid blocks which yielded good load balance statistics (95% or better) for up to 512 processors. Several views of the grid are shown in Fig. 5. The grid was clustered to the isolator surfaces, primary injector surfaces, and combustor side wall surfaces to allow the no-slip boundary condition to be applied directly (*i.e.* y^+ values were near unity). The grid was clustered less aggressively to all remaining no-slip surfaces to reduce the grid cell count required for the simulations. The wall matching procedure of Wilcox [25] was enabled for these surfaces with y^+ values that varied between 15 and 35 for the fine grid. The wall temperature was specified by balancing the heat flux at the wall with the wall-normal heat flux through the surface given a back-side temperature at some known depth. This steady-state treatment was supported by thermocouple time histories recorded during the tests. The isolator and combustor surfaces were made of copper with a thin zirconia coating for added thermal protection. The data required to set the thermal boundary condition for these surfaces were obtained from embedded wall thermocouples present at various locations in the isolator and combustor. The facility nozzle was water cooled and made of copper without any zirconia coating. The back-side temperature for these surfaces was iteratively varied until the global heat loss through the nozzle matched what was experimentally determined. The resulting conditions are given in Table 2.

Table 2: HDCR surface thermal conditions

Surface	t/k [m^2 K / Watts]	Back-side Temperature [K]
Nozzle	8.170×10^{-6}	600.0
Isolator	4.307×10^{-4}	350.0
Combustor	4.307×10^{-4}	500.0

The 4 species tracked in the CFD simulations were O_2, N_2, *Fuel*, and *Prod*. The *Fuel* species was a 64%
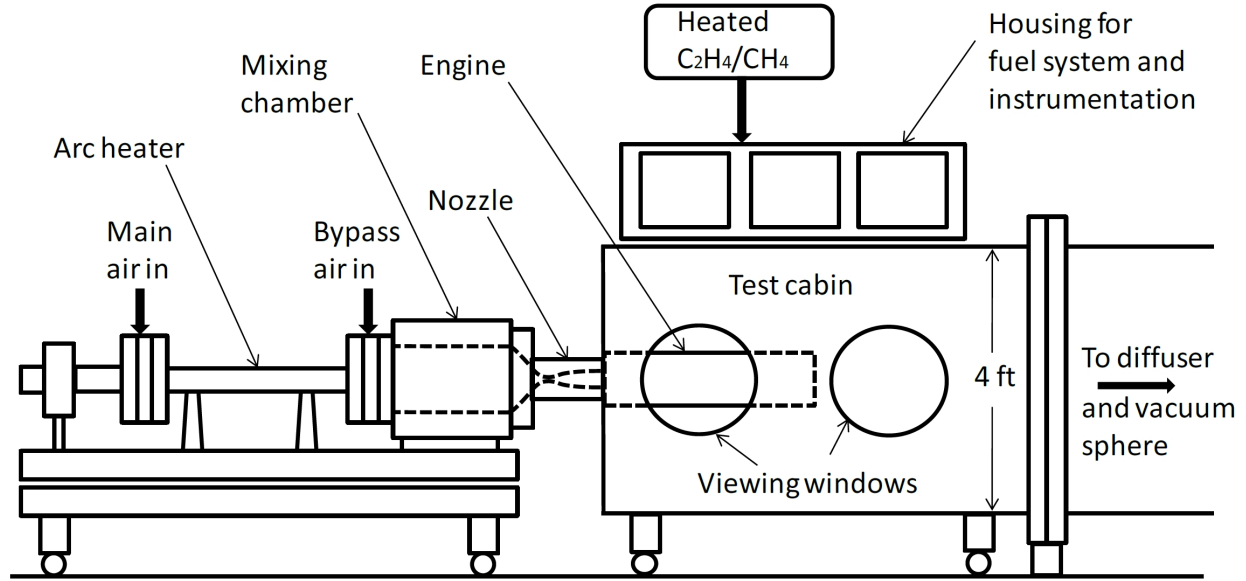
Figure 3: Schematic of the HDCR installation

ethylene - 36% methane mixture (by mole) that was designed to be a surrogate for endothermically-cracked JP-7. [26] The *Prod* species was a 54.945% steam - 45.055% carbon dioxide mixture (by mole) that results from the stoichiometry of the fuel-air system. The individual components of the *Fuel* and *Prod* species were not tracked independently due to a lack of reliable translation/vibration relaxation time data for ethylene and steam. Instead, the Millikan and White translation/vibration relaxation time parameters for methane and carbon dioxide were used for the *Fuel* and *Prod* species, respectively. Steam is known to promote very rapid thermal equilibration even when present in small quantities. This effect was accounted for to some extent through specialized Millikan and White parameters that were extracted from Ref. [27], where the vibrational relaxation of nitrogen in the presence of steam was measured. All other translation/vibration relaxation time parameters were taken from the database distributed with the Langley Aerothermodynamic Upwind Relaxation Algorithm CFD code. [13] Table 3 lists the Millikan and White relaxation time parameters used for this effort. The preferential dissociation constant, C_{pd} (see Eq. 14 in Appendix A), was set to unity for the combusting simulations.

Table 3: Translation/Vibration Millikan and White relaxation time parameters

Molecule	A_{mN_2} , B_{mN_2}	A_{mO_2} , B_{mO_2}	A_{mFuel} , B_{mFuel}	A_{mProd} , B_{mProd}
N_2	220.0 , *	220.0 , *	220.0 , *	21.0 , 0.81286
O_2	129.0 , *	129.0 , *	129.0 , *	129.0 , *
$Fuel^a$	314.3 , *	314.3 , *	314.3 , *	314.3 , *
$Prod^b$	270.4 , *	270.4 , *	270.4 , *	270.4 , *

* Denotes the default Millikan and White value for B_{mn}
[a] Millikan and White relaxation data taken to be that of CH_4
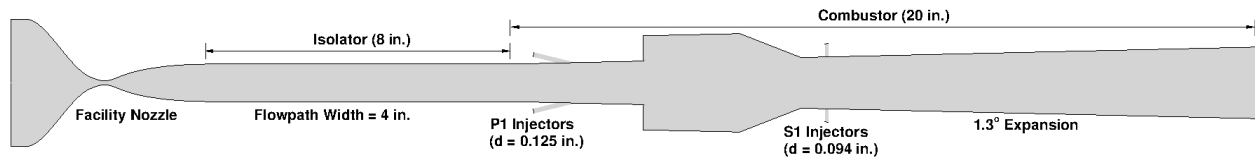[b] Millikan and White relaxation data taken to be that of CO_2

Figure 4: HDCR facility flowpath (the 8 P1 and 8 S1 injectors are evenly spaced across the flowpath width)
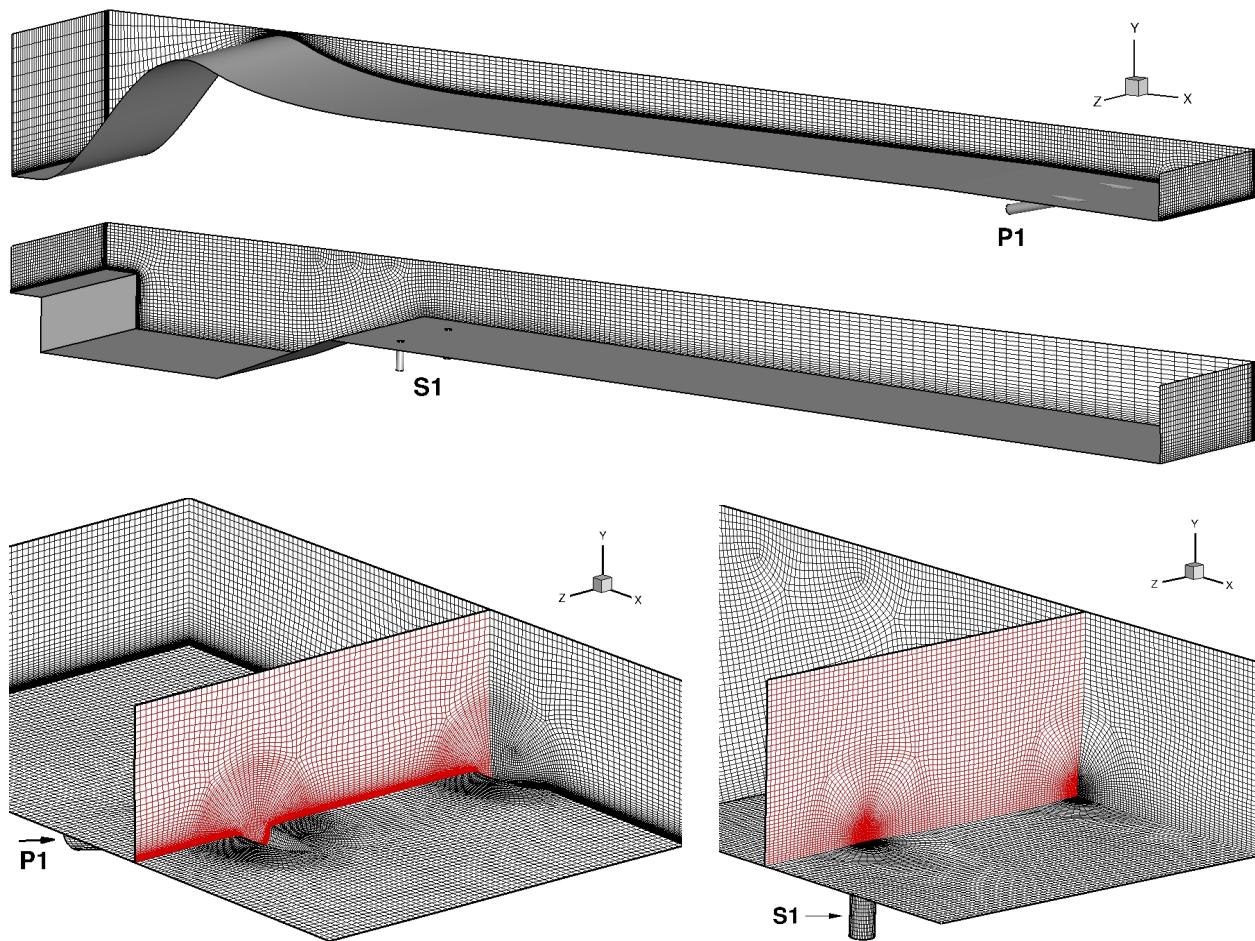

Figure 5: HDCR grid images: entire flowpath with every other grid point removed for clarity (top 2 images), primary fuel injection region (bottom left), secondary fuel injection region (bottom right)

RESULTS AND DISCUSSION

Vibrational freezing was most pronounced in the Mach 8 tests of the HDCR flowpath, so this effort focused on the Mach 8 test series. Both tare and combusting simulations were performed for the conditions listed in Table 4 (these conditions correspond to facility Run number 136.3). For each flow condition, both thermal equilibrium and thermal non-equilibrium gas models were considered. Solution convergence was monitored by assessing the L_2 norm of the steady-state equation set residual error, the mass flow error, and the integrated surface heat load time history. At a minimum, the following iterative convergence statements were satisfied for each simulation:

- The L_2 norm of the steady-state residual error was reduced by at least 4 orders of magnitude.

- The integrated surface load time histories were unchanged to at least 4 significant digits over the last 20000 iteration cycles.

- The integrated mass flow rate was balanced out and constant at every streamwise grid plane to at least 4 significant digits.

Fig. 6 shows a typical convergence history for both thermally equilibrated and thermal non-equilibrium simulations.

Table 4: HDCR facility flow conditions

Facility condition	Tare	Reacting
Nozzle $P_\circ$ [kPa]	4117.575	4276.818
Nozzle $\dot{m}$ [kg/s]	0.90083	0.91218
Equivalence Ratio	N/A	0.988
Primary fuel $\dot{m}$ [kg/s]	N/A	0.02359
Primary fuel $T_\circ$ [K]	N/A	290.64
Secondary fuel $\dot{m}$ [kg/s]	N/A	0.03538
Secondary fuel $T_\circ$ [K]	N/A	298.36
Secondary fuel Mach no.	N/A	1.0

The level of thermal non-equilibrium present in the tare and combusting simulations are illustrated in Fig. 7. In these images, the vibrational/electronic temperature is plotted on one side of the centerline, and the translational/rotational temperature is plotted on the other. The spanwise plane shown is the $z/h = 0.5$ slice (h is the isolator height equal to 1 inch) that bisects the inboard injection ports. Vibrational freezing is seen to initiate near the facility nozzle throat where the expansion is too rapid for the molecular collision frequency to maintain thermal equilibrium. At the exit of the nozzle, the vibrational/electronic temperature is nearly 1150 K higher than the temperature associated with the translational/rotational modes. As the flow travels through the constant area isolator, the translational/rotational temperature gradually increases due to boundary layer growth along the walls, and weak shock reflections that result due to inexact wave cancellations during the nozzle expansion process. The vibrational/electronic temperature gradually decreases as this energy mode relaxes towards equilibrium with the translational/rotational energy. The tare simulation shows this trend to continue as the flow traverses through the combustor, and the flow remains in a thermal non-equilibrium state throughout the combustor. The thermal equilibration process is quite different for the combusting simulations (right image of Fig. 7). The pressure rise due to heat release forces a strong oblique shock to stabilize just downstream of the primary injectors. The increase in pressure (and temperature) across this shock wave is sufficient to thermally equilibrate the flowfield at this location, resulting in identical vibrational/electronic and translational/rotational temperatures at stations further downstream.

The under-expanded fuel jets also show regions of thermal non-equilibrium as shown in Fig. 8. The temperature range has been clipped at 300 K in these images to reveal the details present in the fuel plumes.
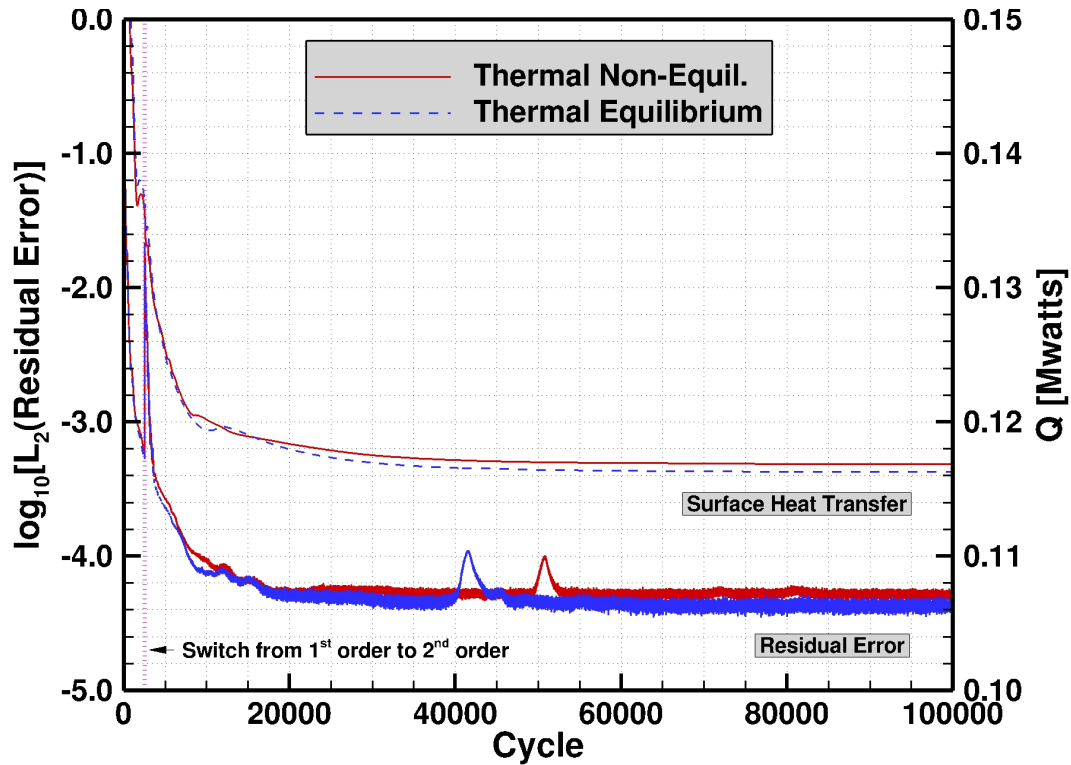
Figure 6: Iterative convergence histories for reacting flow HDCR simulations

The fuel flow in the primary injectors (left image) gradually accelerates due to boundary layer growth along the fuel pipes, resulting in a continuous decrease in the translational/rotational temperature until the choke point is reached. A weak three-dimensional compression wave is present shortly downstream of the choke point followed by continued expansion to supersonic jet plume conditions. The vibrational/electronic temperature (shown in the upper half of the combustor) remains frozen at the inflow value until mixed with the hot air stream. The temperature fields associated with the secondary injectors are shown in the right image of Fig. 8. Slip walls were assumed in the secondary injection ports, so the vibrational/electronic energy remains equilibrated with the translational/rotational energy as the flow simply convects through the ports. However, upon entering the combustor the under-expanded fuel rapidly plumes outward resulting in a sharp drop in the translational/rotational temperature. The vibrational modes do not have sufficient time to equilibrate during this short duration and the vibrational/electronic temperature remains frozen at the inflow value until being mixed with the hot incoming air. It should be emphasized that vibrational relaxation coefficients for ethylene were not available for these simulations, and the relaxation data available for methane may be unreliable. Hence, the observations extracted from these simulations must be balanced with the known limitations of the data used to obtain these results.

The flow structure of the thermal non-equilibrium tare and reacting solutions are compared to that obtained by assuming thermal equilibrium in Fig. 9. In these images, the thermal equilibrium results are shown on one side of the centerline, while the thermal non-equilibrium results are shown on the other. The first notable difference is the higher Mach number (based on the sonic speed given by the translational/rotational specific heat ratio) near the nozzle exit that results due to vibrational freezing. Moreover, the facility nozzles used for the HDCR tests were designed using thermal equilibrium CFD models. Hence, the thermally equilibrated flow in the supersonic portion of the nozzle is nearly shock-free, while non-negligible shock reflections are clearly present due to the vibrational freezing not accounted for in the nozzle design process. As will be shown later, these shock reflections are evident in the surface pressures measured in the isolator. The non-equilibrium tare results show a somewhat stronger expansion into the cavity due to the higher approach Mach number, resulting in a slight difference in the alignment of shock reflections through the combustor as
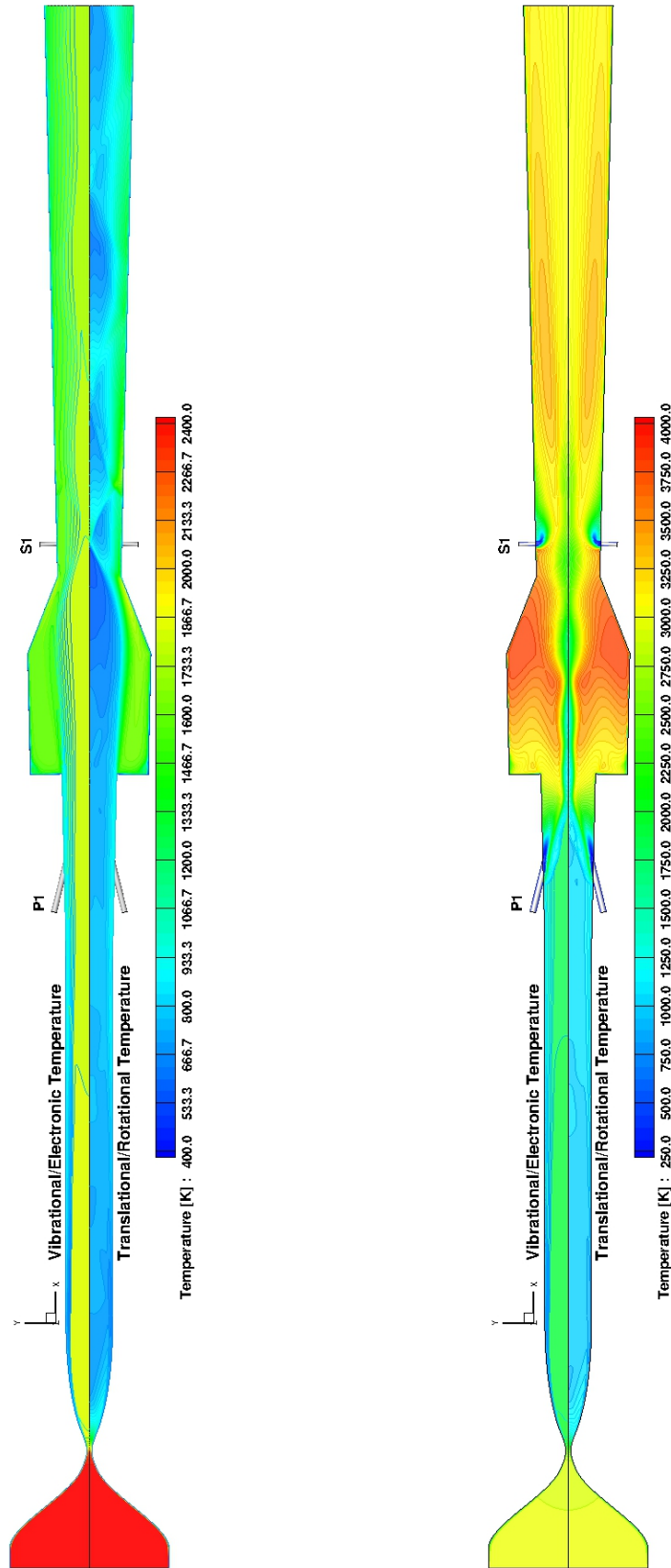
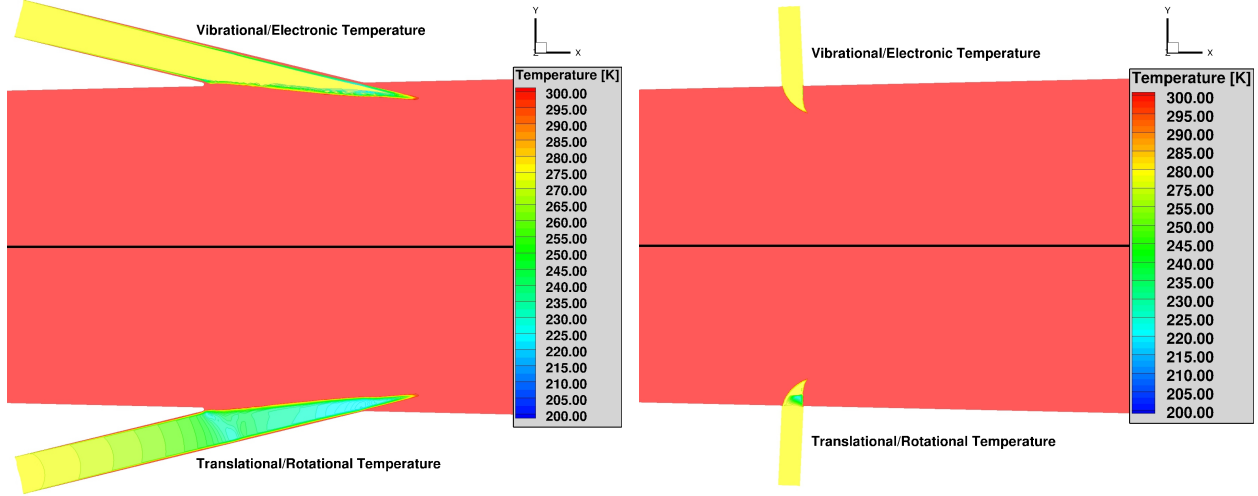Figure 7: Temperature contours: tare T_{ve} and T_{tr} (left), combusting T_{ve} and T_{tr} (right)

Figure 8: Fuel temperature contours: P1 injector T_{ve} and T_{tr} (left), S1 injector T_{ve} and T_{tr} (right)

compared with the thermally equilibrated results. The combusting results (right image of Fig. 9) show larger differences in the injector nearfield, with less differences noted in the combustor farfield. In particular, the recirculation region just downstream of the primary injectors, where the combustion-induced shock wave is located, is significantly smaller for the thermally equilibrated results. This affects how the core flow is diverted into the cavity, altering how the flow interacts with the cavity flameholder. The larger separation bubble at the combustion-induced shock location seen in the thermal non-equilibrium results is likely due to the elevated approach flow Mach number. For a given level of heat release, a higher supersonic Mach number results in a larger pressure increase, strengthening the adverse pressure gradient as compared with the thermally equilibrated flowfield.

Initial comparisons of the computed wall pressure data to measurements near the nozzle exit (isolator entrance) showed that the pressure was overpredicted by 7 - 8% even when accounting for thermal non-equilibrium. Discussions with the experimental team revealed that a nozzle leak was discovered while performing hardware integrity checks after the Phase I tests. An identical facility nozzle was available and installed for the Phase II testing, and tests at conditions that nominally matched Run number 136 were repeated. A comparison of the measured stagnation pressure to isolator entrance pressure (P_1) ratio of this test (Run 207) with that of Run 136 revealed a difference of 6.9%; a disparity very close to that noted in the initial CFD comparisons. To account for the apparent pressure loss due to a nozzle leak, the measured pressures of Run 136 were offset based on the following expression:

$$ P = \left(P - P_1^{236} \right) + P_\circ^{136} \left(\frac{P_1^{207}}{P_\circ^{207}} \right) \tag{4} $$

The resulting comparison of surface pressure with measurements along the $z/h = 0$ HDCR centerplane is shown in Fig. 10. The error bars associated with the CFD data represents the numerical uncertainty estimate as calculated from the GCI. This comparison confirms the presence of vibrational freezing in the facility as evidenced by the marked improvement in the pressure comparison in the isolator (the assumption of thermal equilibrium results in a nozzle exit pressure that is nearly 20% larger than the measured value). Moreover, the isolator wave structure shown in the thermal non-equilibrium pressure distribution closely mimics that of the measured data (the trend is more clearly visualized in the combusting flow comparisons discussed below). The tare data comparison shows very little differences in the location of the pressure peaks and valleys in the combustor nearfield. However, the larger Mach numbers in the thermal non-equilibrium results produce shallower shock angles that shift the pressure peaks and valleys further downstream as compared to the thermally equilibrated results. Note also the systematic increase in the numerical uncertainties at stations further downstream. This trend is typical of flows with multiple shock
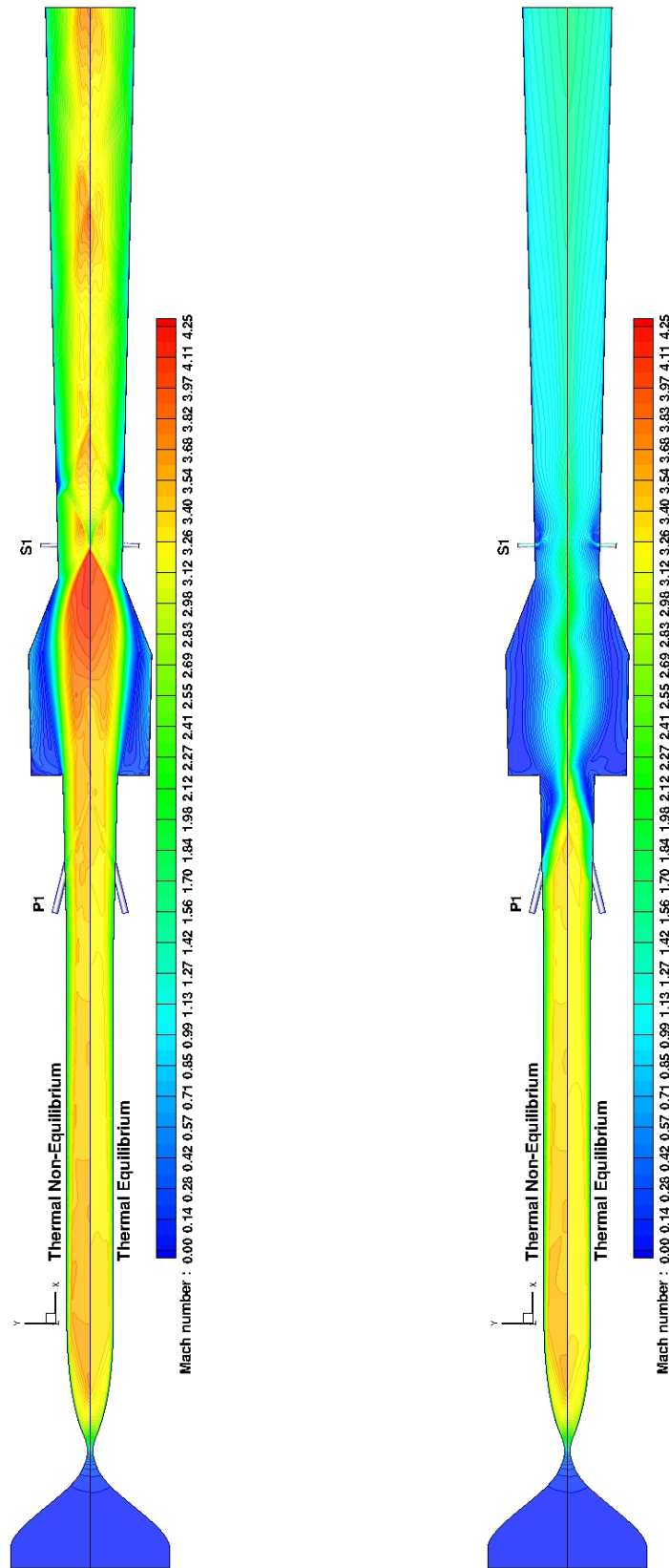
Figure 9: Mach number contours: tare thermal non-equilibrium and thermal equilibrium results (left), combusting thermal non-equilibrium and thermal equilibrium results (right)

reflections where slight changes in shock position lead to large local pressure differences between grid levels. Alternatively, one could choose to track the numerical error for shock-dominated flows based on shock position rather than the raw pressure values. This approach is particularly useful when a small number of steep shock waves are present as was the case for the combusting simulations performed here. The numerical uncertainty for the combusting simulation results was quantified by applying both of these metrics. The numerical errors in the vicinity of the combustion-induced shock wave were tracked as a shock position uncertainty (shown as a horizontal uncertainty bar in the lower image of Fig. 10), while outside of this region the numerical uncertainty was tracked as a raw pressure uncertainty. The presentation of the uncertainties in this way clearly displays the trend that an increase in grid resolution shifts the incident shock wave further upstream while increasing the post-shock pressure levels. In general, accounting for thermal non-equilibrium effects shifted the combustion-induced shock wave further upstream (consistent with the measurements) along with elevating the pressures downstream as compared with the thermally equilibrated results.

The impact of thermal non-equilibrium on various performance metrics of interest (P_o^{rec} and η_c) are shown in Fig. 11. The total pressure recovery and the combustion efficiency (based on fuel depletion) are defined as follows:

$$P_o^{rec} = \frac{\int P_o \, \rho \, u_j \, n_j \, dA}{P_o^{ref} \int \rho \, u_j \, n_j \, dA} \, , \qquad \eta_c = 1 \, - \, \frac{\int Y_{fuel} \, \rho \, u_j \, n_j \, dA}{\dot{m}_{fuel}^{inj}} \tag{5}$$

where the integration is performed over all cell faces at the streamwise plane of interest. The reference total pressure, P_o^{ref}, was taken as the facility nozzle plenum pressure, and $\dot{m}_{fuel}^{inj}$ represents the total mass flow of fuel injected into the combustor at or before the streamwise plane of interest. The deficit in P_o^{rec} (4.5% percent difference) at the isolator entrance relative to the thermally equilibrated value is a result of the entropy gain due to vibrational freezing within the nozzle. This deficit is never fully overcome, but the percent difference is reduced to 2.5% at the combustor exit. The combustion efficiency is uniformly higher when thermal non-equilibrium is accounted for. This trend is consistent with the fact that the pressure levels in the combustor are higher than those present when thermal equilibrium is assumed.

The final issue addressed in this effort was the question concerning the applicability of the calibrated CFD model (using ground test data) that was carried forward for the flight simulations. This calibration process was based on thermal equilibrium simulations of ground tests, even though a significant degree of thermal non-equilibrium was present. As a result, there was some concern that the calibrated S_{c_t} value (a parameter that governs the rate of turbulent mixing) may have incorrectly compensated for thermodynamic model deficiencies. As shown in Fig. 10, the calibrated S_{c_t} value of 0.5 (based on a thermal equilibrium assumption) produced combustor pressure levels that were somewhat higher than what the measurements indicate when the thermal non-equilibrium model was employed. Hence, a higher S_{c_t} value might yield a better fit to the data. Two additional simulations ($S_{c_t} = 0.55$ and $S_{c_t} = 0.6$) were undertaken to determine an optimal turbulent Schmidt number for use with the thermal non-equilibrium model. The $S_{c_t} = 0.55$ solution proved to be a better fit, so this value was carried forward as the properly calibrated value for the thermal non-equilibrium flowfield. The surface pressure distributions obtained from both the $S_{c_t} = 0.5$ and $S_{c_t} = 0.55$ simulations are compared to measurements in Fig. 12. While the $S_{c_t} = 0.55$ value provided a better fit to the measurements, the combustion-induced shock position and overall flowfield structure were not significantly different from that obtained using the original $S_{c_t} = 0.5$ value. Hence, the conclusions drawn from the flight simulations performed to date are not expected to be significantly altered by such a small change in the turbulent Schmidt number.
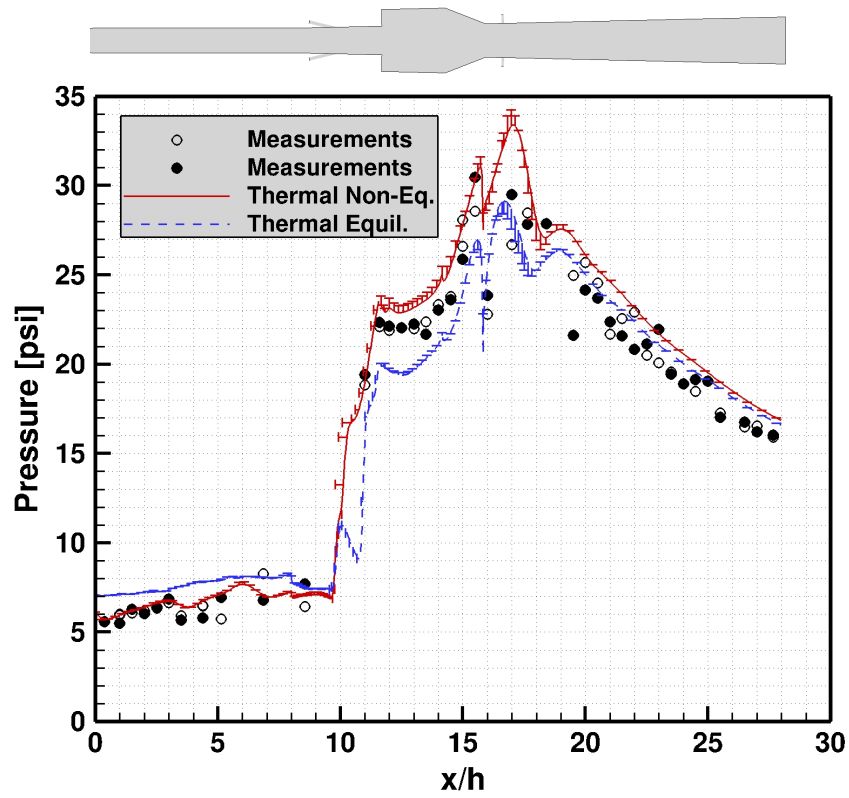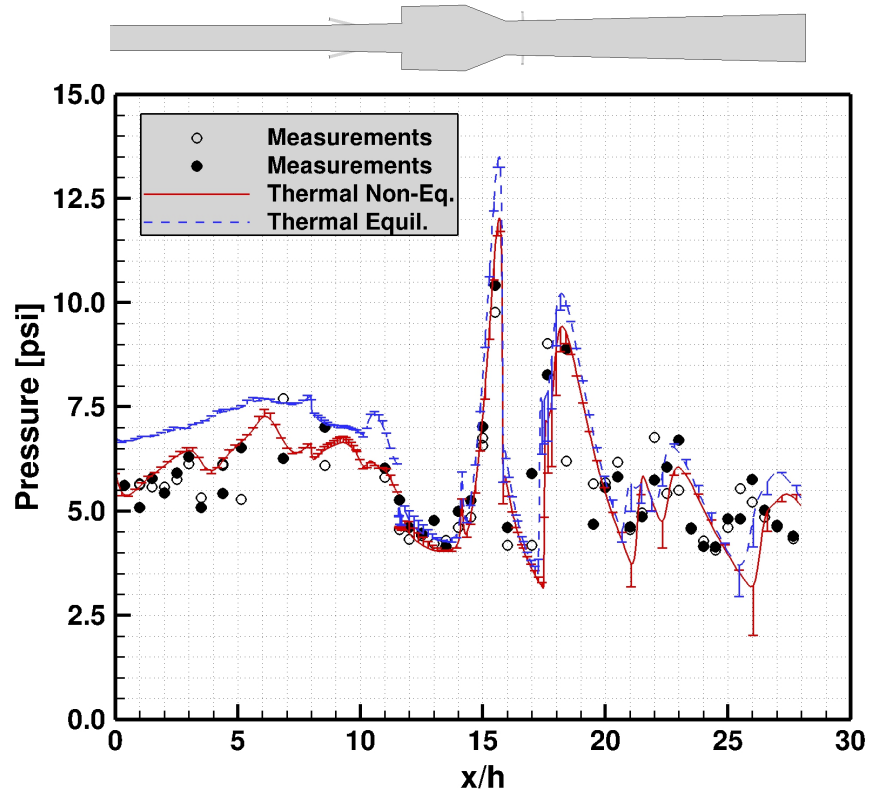
Figure 10: Centerline surface pressure comparisons with measurements (solid and hollow symbols represent opposite walls): tare results (top), combusting results (bottom)
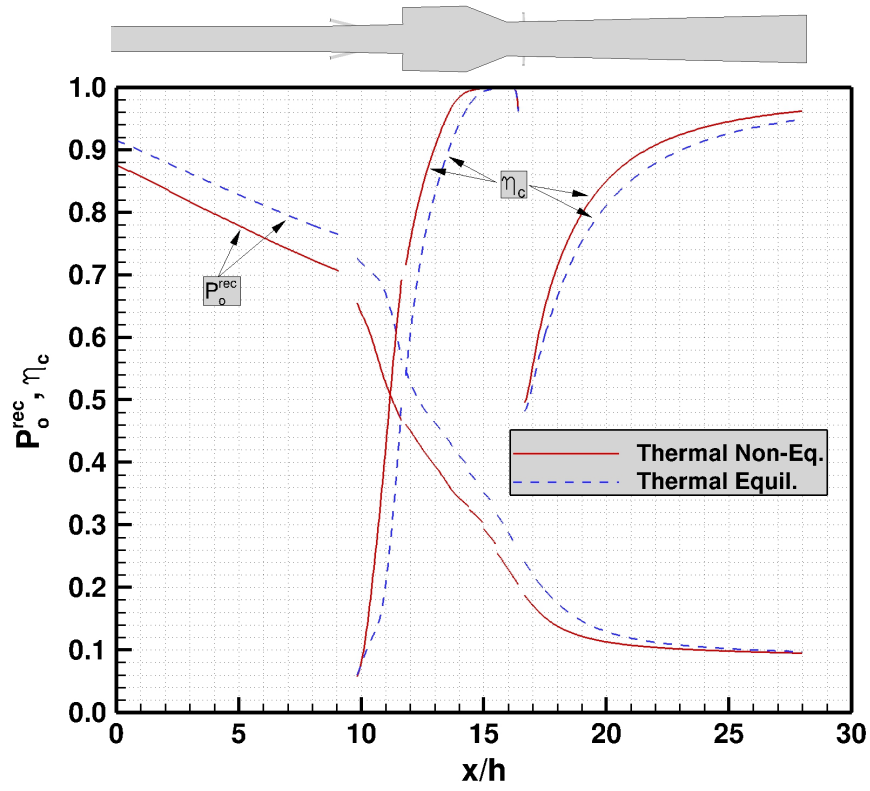
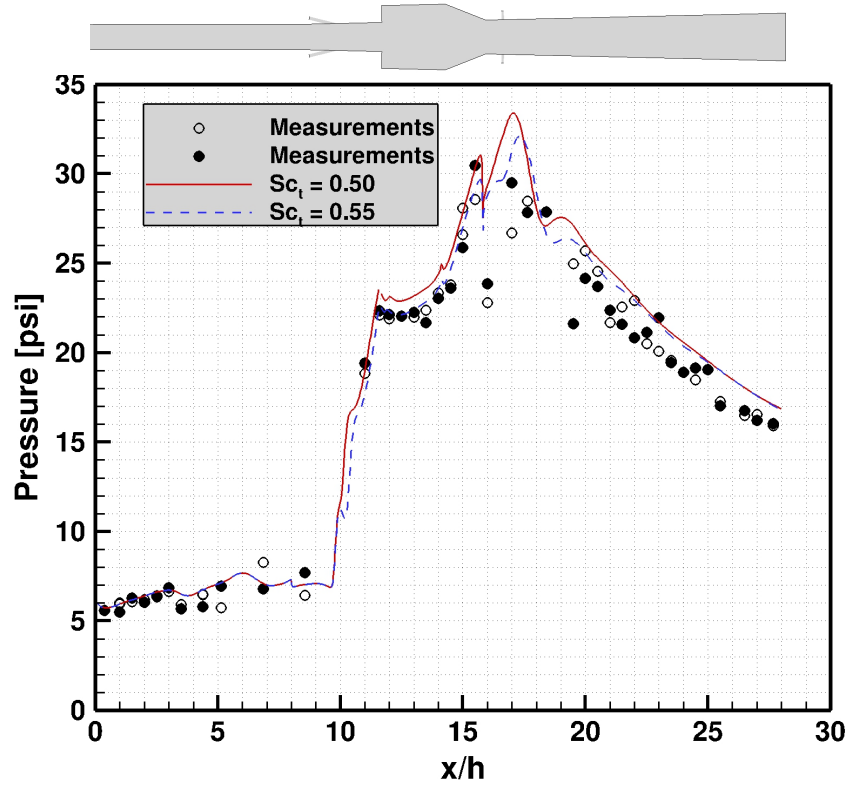Figure 11: Total pressure recovery and combustion efficiency

Figure 12: Centerline surface pressure comparisons with measurements using $S_{c_t} = 0.50$ and $S_{c_t} = 0.55$

SUMMARY

A HIFiRE direct-connect rig CFD analysis was performed to address the impact of thermodynamic non-equilibrium effects. The direct-connect ground tests of the HIFiRE flowpath were performed in the Arc-Heated Scramjet Test Facility located at the NASA Langley Research Center. This facility introduces flow conditions to the scramjet test article that contain some level of thermal non-equilibrium. The thermal non-equilibrium effects (in the form of vibrational freezing) proved to have a non-negligible impact on the thermodynamic state of the flow entering the isolator, particularly at the Mach 8 flight test conditions. This complicated the CFD calibration effort since the CFD analysis performed to support pre-flight activities utilized a thermal equilibrium gas model. The impact of thermal non-equilibrium was modeled in this effort through the use of a two-temperature formulation (translational/rotational and vibrational/electronic temperatures) that was recently added to the VULCAN-CFD code. Overall, comparisons with measured wall pressure data improved significantly when vibrational freezing was accounted for in the simulations. Previous simulations performed using a thermal equilibrium model predicted isolator entrance pressures that were 20% larger than the measured values. Accounting for vibrational freezing reduced this error by an order of magnitude. The vibrational/electronic energy remained in a non-equilibrium state throughout the HDCR flowpath for the tare simulations. The combusting simulations, on the other hand, fully equilibrated shortly after the pre-combustion shock wave (just downstream of the primary injection site).

A comparison of the combusting thermal equilibrium and thermal non-equilibrium solutions showed several notable differences. The first difference was an elevated Mach number produced by the vibrational freezing in the nozzle. The second difference was the appearance of shock reflections in the isolator that result from imperfect wave cancellations in the facility nozzle (the facility nozzle was designed using thermal equilibrium analytic tools). Finally, the combustion-induced incident shock wave was stronger and located further upstream when thermal non-equilibrium was accounted for, resulting in a larger separation zone just downstream of the primary fuel injection site. Each of these specific thermal non-equilibrium flowfield features contributed to an improved comparison with measured surface pressure distributions.

Finally, the impact of accounting for thermal non-equilibrium effects on the calibration process used for ground-to-flight mapping was assessed through a recalibration of the turbulent Schmidt number using the thermal non-equilibrium model for the ground test simulations. This effort resulted in a calibrated turbulent Schmidt number of 0.55 instead of the 0.5 value arrived at under the assumption of thermal equilibrium. While the recalibrated CFD model showed some improvements when comparing wall pressures to measured values, the overall differences in flow structure were minor. Hence, the present findings do not significantly alter the ground-to-flight mapping used for the HIFiRE Flight 2 CFD predictions.

ACKNOWLEDGMENTS

REFERENCES

[1] Jackson, K. R., Gruber, M. R., and Buccellato, S., *HIFiRE Flight 2 Project Overview and Status Update 2011*, AIAA Paper 2011-2202 (April 2011).

[2] Pellet, G. L., Bruno, C., and Chinitz, W., *Review of Air Vitiation Effects on Scramjet Ignition and Flameholding Combustion Processes*, AIAA Paper 2002-3880 (2002).

[3] Srinivasan, S. and Erickson, W. D., *Interpretation of Vitiation Effects on Testing at Mach 7 Flight Conditions*, AIAA Paper 95-2719 (1995).

[4] Thomas, S. R. and Guy, R. W., *Scramjet Testing from Mach 4 to 20 Present Capability and Needs for the Nineties*, AIAA Paper 90-1388 (1990).

[5] Erdos, J. I., *Ground Testing Abilities, Inabilities and Options for Scramjet Development*, AIAA Paper 97-3014 (1997).

[6] Tirres, C., Bradley, M., Morrison, C., and Edelman, R., *A Flow Quality Analysis for Future Hypersonic Vehicle Testing*, AIAA Paper 2002-2706 (2002).

[7] Powell, E. S. and Stallings, D. W., *A Review of Test Medium Contamination Effects on Test Article Combustion Processes*, AIAA Paper 98-0557 (Jan. 1998).

[8] Canupp, P., Candler, G., and Perkins, J., *Analysis of Hypersonic Nozzles Including Vibrational Nonequilibrium and Intermolecuar Force Effects*, AIAA Paper 92-0330 (Jan. 1992).

[9] Nompelis, I., Candler, G. V., and Holden, M. S., *Effect of Vibrational Nonequilibrium on Hypersonic Double-Cone Experiments*, AIAA Journal, 41(11):2162–2169 (Nov. 2003).

[10] Storch, A., Bynum, M., Liu, J., and Gruber, M., *Combustor Operability and Performance Verification for HIFiRE Flight 2*, AIAA Paper 2011-2249 (Oct. 2011).

[11] White, J. A. and Morisson, J. H., *Pseudo-Temporal Multi-Grid Relaxation Scheme for Solving the Parabolized Navier-Stokes Equations*, AIAA Paper 99-3360 (June 1999).

[12] VULCAN, *http://vulcan-cfd.larc.nasa.gov/* (2016).

[13] Gnoffo, P. A., Gupta, R. N., and Shinn, J. L., *Conservation Equations and Physical Models for Hypersonic Air Flows in Thermal and Chemical Nonequilibrium*, NASA Technical Paper 2867 (Feb. 1989).

[14] Cutler, A. D., Cantu, L. M. L., Gallo, E. C. A., Baurle, R. A., Danehy, P. M., Rockwell, R., Goyne, C. and McDaniel, J., *Measurement of Vibrational Non-Equilibrium in a Supersonic Freestream Using Dual-Pump CARS*, AIAA Journal (2015).

[15] Krist, S. L., Biedron, R. T., and Rumsey, C. L., *CFL3D User's Manual (Version 5.0)*, NASA Technical Report TM-1998-208444 (1998).

[16] Edwards, J. R., *A Low Diffusion Flux-Splitting Scheme for Navier-Stokes Calculations*, Computers & Fluids, 26(6):635–659 (1997).

[17] Menter, F. R., *Zonal Two Equation k-ω Models for Aerodynamic Flows*, AIAA Paper 93-2906 (July 1993).

[18] Roache, P. J., *Verification and Validation in Computational Science and Engineering*, Hermosa Publishers (1998).

[19] Winovich, W., *On the Equilibrium Sonic-Flow Method for Evaluating Electric-Arc Air-Heater Performance*, NASA Technical Note 2132 (1964).

[20] Lemmon, E. W., Huber, M. L., and McLindon, M. O., ***REFPROP-Reference Fluid Thermodynamic and Transport Properties***, Nist standard reference database 23, version 8.0 (2007).

[21] van Leer, B., ***Towards the Ultimate Conservation Difference Scheme. II. Monotinicity and Conservation Combined in a Second Order Scheme***, Journal of Computational Physics, 14:361–370 (1974).

[22] McBride, B. J. and Gordon, S., ***Computer Program for Calculation of Complex Chemical Equilibrium Composition and Applications, I. Analysis***, NASA Reference Publication 1311 (Oct. 1994).

[23] McBride, B. J. and Gordon, S., ***Computer Program for Calculation of Complex Chemical Equilibrium Composition and Applications, II. Users Manual and Program Description***, NASA Reference Publication 1311 (June 1996).

[24] Magnussen, B. F. and Hjertager, B. H., ***On Mathematical Modeling of Turbulent Combustion with Special Emphasis on Soot Formation and Combustion***, in *Sixteenth Symposium (International) on Combustion*, pages 719–729 (1976).

[25] Wilcox, D. C., ***Wall Matching, a Rational Alternative to Wall Functions***, AIAA Paper 89-0611 (Jan. 1989).

[26] Pellet, G. L., Dawson, L. C., and Wilson, L. G., ***Nitric Oxide and Oxygen-Air Contamination Effects on Extinction Limits of Non-premixed Hydrocarbon-Air Flames for a HIFiRE Scramjet***, 2009 JANNAF CS/APS/PSHS Joint Meeting (Dec. 2009).

[27] Center, R. E., Wehrmeyer and Newton, J. F., ***Vibrational Relaxation of N_2 by H_2O***, Journal of Chemical Physics, 68(8):3327–3333 (1977).

[28] Vincenti, W. G. and Kruger, C. H., ***Introduction to Physical Gas Dynamics***, John Wiley and Sons (1965).

[29] Sutherland, W., ***The Viscosity of Gases and Molecular Force***, Philosophical Magazine, 36(223):507–531 (1893).

[30] Wilke, C. R., ***A Viscosity Equation for Gas Mixtures***, Journal of Chemical Physics, 18(4):517–519 (1950).

[31] Mason, E. A. and Saxena, S. C., ***Approximate Formula for the Thermal Conductivity of Gas Mixtures***, Physics of Fluids, 1(5):361–369 (1958).

[32] Millikan, R. C. and White, D. R., ***Systematics of Vibrational Relaxation***, Journal of Chemical Physics, 39(12):3209–3213 (1963).

[33] Park, C., ***Assessment of Two-Temperature Kinetic Model for Ionizing Air***, AIAA Paper 87-1574 (1987).

Appendix A. VIBRATIONAL NON-EQUILIBRIUM MODELING AND IMPLEMENTATION

The two-temperature formulation for flows in thermal non-equilibrium assumes that the energy is partitioned as follows:

$$e = \underbrace{(e_t + e_r)}_{e_{tr}} + \underbrace{(e_v + e_e)}_{e_{ve}} \tag{1}$$

This formulation requires only one additional energy equation (as compared to flows in thermal equilibrium) to be integrated for the vibrational/electronic energy field. Moreover, if one assumes that the translational and rotational energy modes are fully excited (implying that their specific heats are independent of temperature), then the same polynomial fits [22, 23] for thermodynamic properties used for flows in thermodynamic equilibrium can be utilized, which greatly simplifies the thermodynamic relationships as compared with non-equilibrium formulations that permit additional degrees of freedom. For instance, the vibrational/electronic heat capacities for species "m" can be obtained by simply evaluating the polynomial fit for the specific heat with the vibrational/electronic temperature and subtracting out the constant translational and rotational mode contributions, $i.e.$

$$C_{p_{ve,m}} = C_{p_m}(T_{ve}) - C_{p_{tr,m}} \tag{2}$$

Similarly, the vibrational/electronic enthalpy for each species can be obtained by evaluating the polynomial fit for enthalpy using the vibrational/electronic temperature and subtracting out the translational and rotational mode contributions:

$$h_{ve_m} = h_m(T_{ve}) - C_{p_{tr,m}}\left(T_{ve} - T_{ref}\right) - h_m^\circ \tag{3}$$

The vibrational/electronic standard state entropy for each species can be obtained in a similar fashion:

$$s_{ve_m} = s_m(T_{ve}) - C_{p_{tr,m}} ln\left(\frac{T_{ve}}{T_{ref}}\right) - s_m^\circ \tag{4}$$

The two-temperature formulation also offers a convenient means to evaluate the molecular transport properties. The molecular viscosity only depends on the translational/rotational temperature, so it is computed in the same manner as that for flows in thermal equilibrium. However, the thermal conductivity contains independent translational/rotational and vibrational/electronic contributions, $i.e.$

$$k_m = k_{tr,m} + k_{ve,m} \tag{5}$$

The vibrational/electronic thermal conductivity of each species can be derived via the method suggested by Eucken, [28] which assumes that molecular transport of the internal energy modes (rotational, vibrational, and electronic) are not correlated with the velocity. As a result, the molecular transport of the internal energy modes is similar to that of momentum transport, allowing the vibrational/electronic thermal conductivity for species "m" to be expressed as

$$k_{ve,m} = \mu_m C_{p_{ve,m}} \tag{6}$$

The translational/rotational thermal conductivity for species "m" can then be obtained from:

$$k_{tr,m} = k_m(T_{tr}) - \mu_m\left(C_{p_m}(T_{tr}) - C_{p_{tr,m}}\right) \tag{7}$$

where the functional form for k_m is the desired species conductivity model ($e.g.$ specified P_r, Sutherland, [29] McBride polynomial, [22, 23] etc.). The mixture-averaged conductivities for each energy mode are then evaluated based on the desired mixture formula ($e.g.$ Wilke, [30] Mason/Saxena, [31] etc.)

The Reynolds-averaged equation that governs the evolution of the equilibrated vibrational/electronic energy:

$$\underbrace{\frac{\partial}{\partial t}(\bar\rho\tilde e_{ve})}_{1} + \underbrace{\frac{\partial}{\partial x_j}\left(\bar\rho\tilde e_{ve}\tilde u_j + \bar\rho\widetilde{e_{ve}''u_j''}\right)}_{2} = \underbrace{-\frac{\partial\bar q_{ve_j}}{\partial x_j}}_{3} + \underbrace{\sum_{m=1}^{nm}\overline{\rho_m\left(\frac{e_{ve,m}^* - e_{ve,m}}{\tau_m}\right)}}_{4} + \underbrace{\sum_{m=1}^{nm}\overline{\dot w_m\hat D_m}}_{5} -$$

$$\underbrace{\overline{p_e\frac{\partial u_j}{\partial x_j}}}_{6} + \underbrace{\overline{2\,\rho_e\frac{3}{2}(T - T_{ve})\sum_{m=1}^{ns}\frac{\nu_{e,m}}{W_m}}}_{7} - \underbrace{\sum_{m=1}^{ni}\overline{\dot n_{e,m}\hat I_m}}_{8} - \underbrace{\overline{Q}_{rad}}_{9} \tag{8}$$

contains several terms that require closure. The first term requiring closure is the Reynolds vibrational/electronic heat flux vector, $\bar{\rho}\widetilde{e_{ve}''u_j''}$, which is modeled in this effort by the gradient diffusion approximation, *i.e.*:

$$\bar{\rho}\widetilde{e_{ve}''u_j''} = -\frac{\mu_t}{P_{r_t}}\frac{\partial \tilde{e}_{ve}}{\partial x_j} \tag{9}$$

The Reynolds-averaged heat flux vector, $\bar{q}_{ve_j}$, accounts for both heat conduction due to vibrational temperature gradients and the transfer of vibrational/electronic enthalpy due to gradients in species composition. Fick's law of diffusion is used for this latter effect along with the assumption that all specie diffuse at the same rate, *i.e.*

$$\begin{aligned}\bar{q}_{ve_j} &= \overline{-k_{ve}\frac{\partial T_{ve}}{\partial x_j} - \rho D \sum_{m=1}^{ns} h_{ve,m}\frac{\partial Y_m}{\partial x_j}} \\ &\approx -k_{ve}(\tilde{T}_{tr},\tilde{T}_{ve},\tilde{Y}_m)\frac{\partial \tilde{T}_{ve}}{\partial x_j} - \bar{\rho}D(\tilde{T}_{tr},\tilde{Y}_m)\sum_{m=1}^{ns} h_{ve,m}(\tilde{T}_{tr},\tilde{T}_{ve},\tilde{Y}_m)\frac{\partial \tilde{Y}_m}{\partial x_j}\end{aligned} \tag{10}$$

Note that the assumptions used to model $\bar{q}_{ve_j}$ are consistent with how VULCAN-CFD models the total heat flux vector. The Landau-Teller vibrational/translational energy relaxation process is modeled as follows:

$$\sum_{m=1}^{nm}\overline{\rho_m\left(\frac{e_{ve,m}^* - e_{ve,m}}{\tau_m}\right)} \approx \sum_{m=1}^{nm}\bar{\rho}_m\left(\frac{e_{ve,m}(\tilde{T}_{tr}) - e_{ve,m}(\tilde{T}_{ve})}{\bar{\tau}_m}\right) \tag{11}$$

where the vibrational relaxation time of molecule "m" ($\bar{\tau}_m$) is evaluated using a generalized form of the semi-empirical correlation developed by Millikan and White: [32]

$$\bar{\tau}_m \approx \frac{\sum_{n=1}^{ns}\frac{\tilde{Y}_n}{W_n}}{\bar{p}\,\sum_{n=1}^{ns}\frac{\tilde{Y}_n}{W_n}\left(exp\left[A_{mn}\left(\tilde{T}_{tr}^{-\frac{1}{3}} - B_{mn}\right) - 18.42\right]\right)^{-1}} \tag{12}$$

where the pressure, $\bar{p}$, has units of atm. The coefficients A_{mn} and B_{mn} are by default given by the following Millikan and White formulas

$$A_{mn} = 1.16 \times 10^{-3}\,\mu_{mn}^{\frac{1}{2}}\,\theta_{v,m}^{\frac{4}{3}} \tag{13a}$$

$$B_{mn} = 0.015\,\mu_{mn}^{\frac{1}{4}} \tag{13b}$$

However, these values can be overridden if a better fit is known from experimental data. The creation (or destruction) of vibrational energy due to chemical reactions is modeled as

$$\sum_{m=1}^{nm}\overline{\dot{w}_m\hat{D}_m} \approx \sum_{m=1}^{nm}\dot{w}_m(\tilde{T}_{tr},\tilde{T}_{ve},\tilde{\rho}_m)\left(C_{pd}\,e_{ve,m}(\tilde{T}_{ve})\right) \tag{14}$$

where the chemical production rates are evaluated using the two-temperature model of Park, [33] and C_{pd} is a constant greater than or equal to unity. A value greater than unity produces a preferential dissociation effect where molecules in a higher vibrational state are "preferentially" dissociated as compared to those in a lower vibrational state. The remaining terms in Eq. 8 (terms 6 - 9) are non-zero only when free electrons are present which was not the case for the simulations performed in this effort.